

**A New Look At Carbon Abundances in Planetary Nebulae. III.  
DDDM1, IC 3568, IC 4593, NGC 6210, NGC 6720, NGC 6826, &  
NGC 7009**

K.B. Kwitter<sup>1</sup>

Department of Astronomy, Williams College, Williamstown, MA 01267;

kkwitter@williams.edu

and

R.B.C. Henry<sup>1</sup>

Department of Physics & Astronomy, University of Oklahoma, Norman, OK 73019;

henry@phyast.nhn.uoknor.edu

Received \_\_\_\_\_; accepted \_\_\_\_\_

Submitted to the Astrophysical Journal

---

<sup>1</sup>Visiting Astronomer, Kitt Peak National Observatory, National Optical Astronomy Observatories, which is operated by the Association of Universities for Research in Astronomy, Inc. (AURA) under cooperative agreement with the National Science Foundation.

## ABSTRACT

This paper is the third in a series reporting on a study of carbon abundances in a carefully chosen sample of planetary nebulae representing a large range in progenitor mass and metallicity. We make use of the IUE Final Archive database containing consistently-reduced spectra to measure line strengths of C III]  $\lambda$ 1909 along with numerous other UV lines for the planetary nebulae DDDM1, IC 3568, IC 4593, NGC 6210, NGC 6720, NGC 6826, & NGC 7009. We combine the IUE data with line strengths from optical spectra obtained specifically to match the IUE slit positions as closely as possible, to determine values for the abundance ratios He/H, O/H, C/O, N/O, and Ne/O. The ratio of C III]  $\lambda$ 1909/C II  $\lambda$ 4267 is found to be effective for merging UV and optical spectra when He II  $\lambda$ 1640/ $\lambda$ 4686 is unavailable. Our abundance determination method includes a 5-level program whose results are fine-tuned by corrections derived from detailed photoionization models constrained by the same set of emission lines. All objects appear to have subsolar levels of O/H, and all but one show N/O levels above solar. In addition, the seven planetary nebulae span a broad range in C/O values. We infer that many of our objects are matter bounded, and thus the standard ionization correction factor for N/O may be inappropriate for these PNe. Finally, we estimate C/O using both collisionally-excited and recombination lines associated with C<sup>+2</sup> and find the well established result that abundances from recombination lines usually exceed those from collisionally-excited lines by several times.

*Subject headings:* ISM: abundances – planetary nebulae: general – stars: evolution

## 1. Introduction

We report further on a project whose aim is to determine the stellar yield of carbon as a function of stellar mass and metallicity for intermediate-mass stars, those in the mass range  $0.8 < M < 8M_{\odot}$ . These stars are predicted to produce as much as 50% of the carbon in the Galaxy (Henry, Kwitter, & Buell 1998). In our general study, measured line intensities are used in 5-level atom and photoionization model calculations to determine the abundance ratio of C/O in particular, but also of He/H, O/H, N/O, and Ne/O for 22 planetary nebulae (PNe) selected to represent a broad range in progenitor mass and metallicity. Ultimately, we will use our abundance results as constraints for our own stellar evolution models in order to derive the stellar yield of carbon as a function of these two parameters. We have measured IUE spectra of PNe containing strong, collisionally-excited carbon emission lines, spectra which have been re-reduced in a systematic way and are now in the Final Archive. In two earlier papers, the UV data were joined with optical data from the literature; beginning with this paper, we use new optical data acquired specifically for this project.

In our first paper (Henry, Kwitter, & Howard 1996; hereafter Paper I) we listed our sample objects, described our project in detail, and presented results for the first four PNe. In our second paper (Kwitter & Henry 1996; hereafter Paper II) we reported on five additional PNe. In the current paper we describe our analysis of seven more objects: DDDM1, IC 3568, IC 4593, NGC 6210, NGC 6720, NGC 6826, & NGC 7009. Future papers will report on the remaining six objects, as well as present and discuss stellar model predictions of carbon yields for intermediate-mass stars. Section § 2 describes the data used in the analysis of these seven objects; the abundance calculations and results are presented in § 3; and a summary is contained in § 4. More detailed discussion of the project and procedures can be found in Paper I.

## 2. The Data

### 2.1. Optical Observations

The optical data were obtained at KPNO during 18-21 May 1996 with the 2.1m Goldcam CCD spectrometer. The chip is a Ford  $3K \times 1K$  CCD with  $15\mu$  pixels. We used a  $5''$ - wide slit that extended  $285''$  in the E-W direction, with a spatial scale of  $0''.78/\text{pixel}$ . Using a combination of two gratings, we obtained spectral coverage from  $3700\text{-}9600\text{\AA}$  with overlapping coverage from  $\sim 5750 - 6750\text{\AA}$ . Wavelength dispersion was  $1.5\text{\AA}/\text{pixel}$  ( $\sim 8\text{\AA}$  FWHM resolution) for the blue,  $1.9\text{\AA}/\text{pixel}$  ( $\sim 10\text{\AA}$  FWHM resolution) for the red. The usual bias and twilight flat-field frames were obtained each night, along with HeNeAr comparison spectra for wavelength calibration and standard star spectra for sensitivity calibration. Since the chip is thinned, it produces interference fringes visible in the red. In our red spectra the fringes appear at the  $\pm 1\%$  level at  $\sim 7500\text{\AA}$  and increase in amplitude with increasing wavelength:  $\pm 1.5\%$  at  $8000\text{\AA}$ ,  $\pm 4.5\%$  at  $8500\text{\AA}$ ,  $\pm 6\%$  at  $9000\text{\AA}$ . However, even at their worst, *i.e.*, at  $\sim 9500$ , the longest wavelength we measure, the fringe amplitude reaches only about  $\pm 7\%$ . Internal quartz flats were taken at the position of each object both before and after the object integrations in anticipation of removing the fringes during data reduction. It turned out, however, that more noise was introduced in this process than was removed; we therefore decided to leave the fringes untouched, and to accept this additional uncertainty in our line intensities longward of  $\sim 7500\text{\AA}$ .

The original images were reduced in the standard fashion using IRAF<sup>2</sup>. Using tasks in the *kpnoslit* package, these two-dimensional spectra were converted to one dimension by

---

<sup>2</sup>IRAF is distributed by the National Optical Astronomy Observatories, which is operated by the Association of Universities for Research in Astronomy, Inc. (AURA) under cooperative agreement with the National Science Foundation.

extracting a specific section along the slit. The location of the extracted section was chosen to maximize the overlap with the IUE slit.

## 2.2. UV Data

All UV spectra used for this project have been obtained from the IUE Final Archive. Spectra in the Final Archive have been systematically and uniformly re-processed by IUE staff using the NEWSIPS algorithms, and represent the best available calibration of these data. The spectra we use are all short-wavelength (SWP), low-dispersion, and large-aperture ( $21''7 \times 9''1$ ) spectra. Table 1 lists the spectra that were measured for each of the seven program objects considered here, along with their integration times.

## 2.3. Slit Positions

The placement of the Goldcam slit in each target PN was chosen to coincide as closely as possible with the location of the best IUE observations for which detailed positional information was available. Since the position angle of the Goldcam slit is fixed at  $90^\circ$  while the IUE slit position angle is not, the quality of the overlap varies and will be described below for each object. We also note that because of the 2:1 relative slit widths, the largest possible overlap of the Goldcam slit onto the IUE slit is  $\sim 50\%$ .

For each object we now describe the IUE and optical observations with regard to slit position. In general, our optical N-S offsets from the central star or the center of the nebula match the IUE N-S offsets; the E-W component (if any) of the IUE offset is matched in the extraction process that creates a one-dimensional spectrum from the appropriate portion of the two-dimensional spectrum.

*DDDM1*: All three of the IUE spectra were centered on the central star, as were our optical spectra. The position angles of the IUE spectra are very similar:  $349^\circ$ ,  $346^\circ$ , and  $345^\circ$ . Since the optical diameter of DDDM1 is  $0''.6$  (Acker et al. 1992), the entire nebula was included in both IUE and optical observations, rendering moot the issue of overlap.

*IC 4593*: Both IUE spectra were centered  $7''$  S of the center of light (which we are assuming to coincide with the center of the nebula), at a position angle of  $120^\circ$ . Our slit was centered  $3''$  S of the nebula center, which we judge to be fair overlap.

*IC 3568*: All three IUE spectra were centered on the central star at position angles of  $13^\circ 6'$ ,  $108^\circ$ , and  $328^\circ$ . Our slit was centered  $4''$  N of the central star, and we judge the overlap to be reasonably good.

*NGC 7009*: Positions for the four IUE spectra we used for NGC 7009 were kindly provided by Dr. F. Bruhweiler (private communication). Position *a* was located  $9''.3$  S,  $9''$  E of the central star, at a position angle of  $139^\circ$ . For position *b*, the IUE slit was  $9''.3$  S,  $3''.5$  W, again at position angle  $139^\circ$ . To cover both of these IUE positions, the Goldcam slit was located  $9''$  S. Position *c* is located  $4''$  N,  $22''$  E, at a position angle of  $334^\circ$  and includes the east ansa. Position *d* is  $4''$  N,  $8''$  E at a position angle of  $139^\circ$ . For both of these positions, the Goldcam slit was placed  $4''$  N. For all four positions in NGC 7009, the overlap is reasonably good.

*NGC 6720*: Position *a* is located  $11''.2$  S,  $16''.6$  E of the central star at position angle  $124^\circ$ . The Goldcam slit was placed  $11''.2$  S, yielding reasonably good overlap. Position *b* is  $16''$  N,  $42''.8$  E at position angle  $295^\circ$ . The Goldcam slit was  $17''.3$  N, giving reasonably good overlap.

*NGC 6210*: Both IUE spectra were positioned  $4''$  N,  $8''$  E at position angle  $10^\circ 5'$ . The Goldcam slit was centered  $4''$  N, producing fair overlap.

*NGC 6826*: Position *a* is 10'' S, 10'' W of the central star at position angle 218°. Position *b* is 9'' S, 5'' E at position angle 58°. For both of these positions, the Goldcam slit was placed 9'' S, and the resulting overlap was good. Position *c* is 10'' N, 10'' E at position angle 218°. The Goldcam slit was 10'' N, with good overlap.

## 2.4. Line Strengths

Strengths of all optical and UV lines were measured using *splot* in IRAF and are reported in Table 2. Fluxes uncorrected for reddening are presented in columns labelled  $F(\lambda)$ , where these flux values have been normalized to  $H\beta=100$  using our observed value of  $F_{H\beta}$  shown in the third row from the bottom of the table. These line strengths in turn were corrected for reddening by assuming that the relative strength of  $H\alpha/H\beta=2.86$  and computing the logarithmic extinction quantity  $c$  shown in the penultimate line of the table. Values for the reddening coefficients,  $f(\lambda)$ , are listed in column (2), where we employed Seaton’s (1979) extinction curve for the UV and that of Savage & Mathis (1979) for the optical.

Because of imperfect spatial overlap between the optical and IUE observations for all but DDDM-1, a final adjustment was made by multiplying the IUE line strengths by a merging factor that was determined from either the theoretical ratio of the He II lines  $\lambda 1640/\lambda 4686$  or the carbon lines C III]  $\lambda 1909$ /C II  $\lambda 4267$ . The calculation of the merging factors is described in Appendix A, and their values are listed in the last row of Table 2.

The columns headed  $I(\lambda)$  list our final, corrected line strengths, again normalized to  $H\beta=100$ . In general, intensities have uncertainties  $\leq 10\%$ ; single colons indicate uncertainties up to  $\sim 25\%$ , and double colons denote doubtful detections with uncertainties up to  $\geq 50\%$ .

### 3. Results

#### 3.1. Electron Temperatures And Densities

Numerous temperature-sensitive line ratios are available in our data, enabling us to sample electron temperatures at different positions along the line-of-sight. For example, [O III] and [N II] temperatures,  $T_{[O\ III]}$  and  $T_{[N\ II]}$ , are given by the intensity ratios  $\lambda 4363/(\lambda 4959+\lambda 5007)$  and  $\lambda 5755/(\lambda 6548+\lambda 6584)$ , respectively. Two other temperatures are  $T_{[O\ II]}$  and  $T_{[S\ II]}$  which can be inferred from the intensity ratios of  $\lambda 7325/\lambda 3727$  and  $\lambda 4072/(\lambda 6716+\lambda 6731)$ , respectively. In addition, the intensity ratio of  $\lambda 6716/\lambda 6731$  is particularly sensitive to electron density, enabling the determination of the [S II] density,  $N_{[S\ II]}$ .

Therefore, we have computed temperatures and densities for each observed position, and the results are listed in Table 3. For each object listed in the first column we provide the temperatures and densities in Kelvins and  $\text{cm}^{-3}$ , respectively, determined from the above ratios. Values for  $T_{[O\ III]}$  and  $T_{[N\ II]}$  could be calculated in all cases. For  $T_{[O\ II]}$  and  $T_{[S\ II]}$ , observed line ratios often implied temperatures in excess of 25,000K, which seemed unlikely to us, and thus we do not report values in those cases. A possible cause of these excessive temperatures could be the tendency to overestimate the strengths of weak lines such as [O II]  $\lambda 7325$  and [S II]  $\lambda 4072$ . Since electron temperatures vary directly with these line strengths, overestimating them would produce temperatures exceeding the actual values.

Based on our assessments of the errors in our line strength measurements, we estimate the following uncertainties in our calculated temperatures and densities:  $T_{[O\ III]} : \pm 500\text{K}$ ;  $T_{[N\ II]} : \pm 1000\text{K}$ , except for IC 3568, IC 4593, NGC 7009c, and all positions in NGC 6826, which are  $\pm 5000\text{K}$ ;  $T_{[O\ II]} : \pm 2000\text{K}$ ;  $T_{[S\ II]} : \pm 4000\text{K}$ ;  $N_{[S\ II]} : \pm 200\ \text{cm}^{-3}$ , except for

IC 3568, which is  $\pm 700 \text{ cm}^{-3}$ .

We note that where multiple observations are available for different positions within a single nebula, e.g. NGC 7009, NGC 6720, and NGC 6826, values for the density or a specific temperature type are quite consistent, particularly in the case of  $T_{[O III]}$ . Also obvious is that the electron temperatures derived from both [O II] and [S II] lines are consistently above those determined from [O III] and [N II]. One possible explanation is the hardening of the radiation field as it passes from the high-ionization zones nearer to the star where [O III] is found, out to the lower-ionization regions where [O II] and [S II] are formed. However, one would think that [N II] should share this behavior, which it apparently does not. Despite the long baselines for both [O II] and [S II] measurements, reddening errors are not to blame for the temperature discrepancy, since in the case of [O II], the auroral lines are redward of the nebular lines, whereas in [S II], it is the nebular lines that are redder than the auroral lines. Finally, we note again that weak line intensities tend to be overestimated, which would result in electron temperatures that are too high.

### 3.2. Abundance Calculations

In this project we are concerned with the abundance ratios of He/H, O/H, C/O, N/O, and Ne/O. Paper I describes our abundance calculation method in detail. Future papers will use our newly acquired optical data to study S/O and Ar/O.

Two distinct methods exist for deriving abundances in nebulae. The first employs measured line strengths for observed ions along with knowledge of electron temperature and density to determine ionic abundances using a set of simultaneous equations. Subsequently, these ionic abundances are converted to elemental abundances by using standard correction factors to account for unobserved ions of an element. The second method involves the

calculation of a detailed photoionization model whose output line strengths match the observed ones as closely as possible. The input elemental abundances used to produce the successful model are then taken to represent the true levels in the real nebula.

Each of these methods has its own drawbacks. In the first instance, the correction factors can be sensitive to nebular properties such as matter- or radiation-boundedness. In the second case, the perennial problem is determining the uniqueness of the model solution. The number of available observational constraints can be different for each member of a sample such as ours. Thus, a systematic approach using only models to analyze a large number of objects suffers from non-uniformity.

For these reasons we have developed a hybrid method in the spirit of Shields et al. (1981). The heart of the method is the use of a photoionization model to improve results from a five-level atom routine. Briefly, for each PN (or for each position within a PN where multiple positions were observed) we compile a set of merged UV and optical line strengths and use the five-level atom routine ABUN to derive an initial set of nebular abundance ratios  $A_{abun}^{PN}(X)$ , where  $X$  is one of the five abundance ratios listed above. We then employ the photoionization code CLOUDY version 84 (Ferland 1990) to construct a nebular model, use ABUN to determine a set of model abundances  $A_{output}^{mod}(X)$  based upon the model output line strengths, and compare these with the actual model input abundance ratios  $A_{input}^{mod}(X)$ . Our final set of abundance ratios  $A_F^{PN}(X)$  for each PN (or each position within a PN) is calculated by assuming that:

$$A_F^{PN}(X) = A_{abun}^{PN}(X)\xi(X) \tag{1a}$$

where

$$\xi(X) = \frac{A_{in}^{mod}(X)}{A_{abun}^{mod}(X)}. \tag{1b}$$

The correction factor  $\xi$  is therefore a gauge of the accuracy of the use of the ionization

correction factor method for determining abundances. The program ABUN, including the sources for atomic data, was described in detail in Paper I. Therefore, we focus on the models used to determine  $\xi$ .

### 3.3. Model Results

Photoionization models were calculated for each slit position in order to reproduce as closely as possible the physical conditions observed along the line-of-sight. Our models were constrained by a set of 10 important diagnostic ratios constructed directly from observed line strengths. These 10 ratios are known to describe the physical conditions of a nebula quite well. Our goal for each object (or position within an object) was to match each observed ratio to within 0.10-0.15 dex, consistent with observational uncertainties. We assumed that the central stars were blackbodies and that the nebula had a uniform density with a filling factor of unity.<sup>3</sup> The inner nebular radius was taken to be 0.032 pc for all models, but the outer radius was treated as a free parameter. In several cases the best matches to the observed line strengths were produced by truncating the model inside the Strömgren radius, i.e. the model nebula was matter-bounded. Other free parameters included the stellar luminosity, nebular electron density, and nebular abundances of helium, oxygen, nitrogen, carbon, neon, and sulfur.

Table 4A summarizes our model results; for each PN (or position within a PN) we list logarithmically the observed and model-predicted values for 10 important diagnostic line

---

<sup>3</sup>While most PNe are known to have filling factors significantly less than unity, the only measurable quantity affected by the filling factor is the nebular luminosity, a parameter we are not using to constrain our models. Thus, using the same filling factor for all of the nebulae in no significant way influences our abundance results.

ratios in the upper section of the table. The first ratio is sensitive to gas-phase metallicity and electron temperature, the second and third to the level of nebular excitation, the fourth and fifth to electron temperature and density, respectively, and the last five to abundance ratios in the order He/H, N/O, S/O, C/O, and Ne/O. The lower section of the table provides important model input parameters: stellar effective temperature ( $T_{eff}$ ), the log of stellar luminosity  $\log(L)$ , electron density ( $N_e$ ), and the inner and outer nebular radii ( $R_o$  and  $R$ ; values of  $R$  which are less than the Strömngren distance, i.e. matter bounded models, are indicated with a footnote). These are followed by six input abundance ratios. (N.B. We emphasize that these abundance ratios are *not* our final abundances for each object, but are the abundances necessary to produce the best model.)

There are several important points about the model results that require discussion. First, we note that, with the exception of DDDM-1, which is spatially unresolved, these models represent the best-fit solutions to a specific line-of-sight position within a nebula; they are *not* models of whole planetary nebulae. Model parameters were varied to match observed quantities. Thus, the stellar luminosity employed in a model may not be a dependable gauge of the true value. In the same way, physical size of a nebula is not necessarily related directly to  $R_o$  and  $R$ . Second, the only major discrepancy between observed and predicted values in Table 4A occurs in IC 4593 for the He II/He I line ratio. Large sections of parameter space were explored in trying to render a match to this and the other ratios observed for IC 4593. We are encouraged, however, by the fact that good matches have been achieved for the nine remaining ratios, and suggest that the lack of agreement between theory and observations for the He ratio is related to a peculiarity in the spectrum of the real central star at the He<sup>+</sup> ionization edge. Third, there is a discrepancy of five orders of magnitude in the luminosities used to model positions *a* and *b* in NGC 6720 (see Table 4A). These values were required to match the greatly different ratios observed for  $\log I_{[O II]}/I_{[O III]}$ . It may be that position *b* is heavily shadowed and hence is characterized

by much lower ionization, compared with the situation at position  $a$ . Finally, we note that for those PNe where more than one line-of-sight position was modelled, i.e., NGC 7009, NGC 6720, and NGC 6826, the input parameters for the individual models agree quite closely, with the major differences occurring for those parameters related to position, i.e.  $L$ , and  $R$ .

Table 4B lists the correction factors  $\xi$  derived from the models, where  $\xi$  is the ratio of the input model abundance of an element to the value derived from the model-predicted line strengths using the program ABUN. A value of unity represents complete consistency between the two abundance sets. Therefore,  $\xi$  is a model-determined gauge of how closely the abundances derived with our 5-level atom program agree with the actual nebular abundances. An inspection of Table 4B indicates that with some exceptions, most frequently for N/O, values for  $\xi$  are within 20% of unity. We have employed footnotes here to indicate those models that are matter-bounded, and the large discrepancies for N/O, all greater than unity, are clearly associated with these models. Since input N/O varies little from model to model (see Table 4A), the large values of  $\xi$  for N/O in these matter-bounded models must be due to the way in which  $[\text{N II}] \lambda 6584$  relative to  $[\text{O II}] \lambda 3727$  changes as one moves outward approaching the Strömngren edge. Truncation results in a quite different line ratio than would be predicted if the model were to extend out to the Strömngren radius. This finding suggests that N/O ratios in matter-bounded nebulae generally are less secure when the standard ionization correction relation for this ratio is used.

### 3.4. Derived Abundances

Our final abundances for the seven PNe studied here are presented in Table 5A and Fig. 1. Results for each position, for those PNe where more than one position was observed, are given along with averages. Abundance values in Table 5A are given on a linear scale. We

point out that our final abundances in Table 5A for any one object are very consistent with the model input abundances given in Table 3A for the same object. Since the abundances in Table 5A are only indirectly connected to the model abundances in Table 4A through the use of a model-derived correction factor, this result is reassuring, albeit not altogether surprising. Our estimated uncertainties, not including systematic effects, are 15% for He/H, O/H, and Ne/O and 30-50% for C/O and N/O. In Table 5A, the last row contains solar values for the corresponding ratios taken from Grevesse & Anders (1989) for comparison, while the last column lists the Peimbert class of each object. Fig. 1 shows our abundance ratios in logarithmic form and normalized to solar values, where averages have been plotted for those PNe where more than one position was observed. Ratios derived in this paper are shown with filled symbols, using symbol shape to represent specific objects as defined in the figure caption. For comparison, abundance ratios taken from the literature (see the figure caption for sources) are shown with open symbols. Representative error bars are given for each abundance ratio to show uncertainties.

Note that our results for He/H, O/H, and Ne/O are very consistent with earlier measurements. All seven PNe have sub-solar O/H, with the halo object DDDM-1 being the most metal-poor, as expected. In addition, Ne/O is close to solar in all objects, consistent with the idea that both of these elements are produced by stars of similar mass.

In the cases of C/O and N/O we see a large spread among our seven objects. Note that all objects have N/O above solar. In addition, C/O is markedly below solar in DDDM-1 and IC 4593 but well above solar in NGC 6720 and NGC 7009. In the case of IC 4593, our derived value of C/O is roughly 20 times smaller than the ones published by Bohigas & Olguín (1996) and French (1983), both of whom used optical recombination lines of carbon in their analysis. Bohigas & Olguín derived their carbon abundance for IC 4593 using the C III  $\lambda$ 4648 line, which is often blended with [O II]  $\lambda$ 4649, while French used both C III

$\lambda 4648$  and (uncertain) C II  $\lambda 4267$  to derive carbon abundances. We note that our C/O value for IC 4593 as estimated from C II  $\lambda 4267$  in Table 5B is consistent with our results from the C III]  $\lambda 1909$  line. Finally, our derived N/O values are higher for most objects, the result of using values for  $\xi$  which are significantly larger than unity.

Straightforward determination of carbon abundances is hindered by the longstanding problem whereby abundances inferred from the C II  $\lambda 4267$  recombination line are consistently several times greater than values determined from the collisionally-excited line C III]  $\lambda 1909$ . (See Rola & Stasińska 1994 for a recent discussion of this problem.) Since we were able to measure  $\lambda 4267$  in our data at most observed locations, we have estimated C/O ratios implied by this line, employing the data for the relevant effective recombination coefficient given in Péquino, Petitjean, & Boisson (1991). Results of this exercise are shown in Table 5B, where for each position listed in column 1 we give  $N(\text{C}^{+2})_{\lambda 4267}/N(\text{C}^{+2})_{\lambda 1909}$ , the predicted ratio of the number density of  $\text{C}^{+2}$ , in column 2. Then, since  $C/O \approx C^{+2}/O^{+2}$  (Rola & Stasińska 1994; Paper 1), we scaled the C/O ratios in Table 5A derived from the  $\lambda 1909$  line by multiplying them by the values in column 2 of Table 5B to arrive at the estimates of recombination C/O reported in column 3. We give results for each observed position along with an unweighted average for those PNe in which we obtained data at more than one location. Numbers in column 2 provide a good comparison of the recombination and collisional excitation methods for inferring C/O. As seen in many previous studies, the recombination method consistently implies a significantly larger value for C/O. However, because of the uniformly weak strength of C II  $\lambda 4267$ , we have adopted the C/O abundances determined from the C III]  $\lambda 1909$  line for the *final* values in our study for this abundance ratio.

A discussion of implications for stellar nucleosynthesis is postponed until abundances for our entire sample have been determined.

#### 4. Summary

This paper is the third in a series reporting on a study of carbon and other abundances in a well-defined sample of planetary nebulae representing a broad range in progenitor mass and metallicity. We have obtained new optical spectra from 3700-9600Å at specific positions in our program objects in order to overlap spatially as nearly as possible with earlier IUE sites. We make use of the Final Archive database of IUE spectra, in which the data have been reduced under a new, consistent system of algorithms. We have measured collisionally-excited emission lines of carbon and coupled these measurements to our new optical line strengths to determine abundance ratios of He/H, O/H, C/O, N/O, and Ne/O for seven PNe: DDDM1, IC 3568, IC 4593, NGC 6210, NGC 6720, NGC 6826, and NGC 7009. IUE and optical spectra for the same line-of-sight position were merged using the ratio He II  $\lambda 1640/\lambda 4686$ , or the C III]  $\lambda 1909/\text{C II } \lambda 4267$  ratio when both He II lines were unavailable. In those positions where both the helium and carbon lines were measurable, we found reasonable consistency between these two methods. To our knowledge, this is the first attempt to use the carbon line ratio for merging UV and optical spectra.

Electron temperatures and densities were determined at all locations. Derived values for different positions within the same nebula were found to be quite consistent.

Nebular abundances were inferred by using a hybrid method which couples an empirical 5-level atom calculation with a photoionization model which is used to fine-tune the ionization correction factor. Thus, a photoionization model was produced for each object in which 10 important diagnostic line ratios were matched satisfactorily. Many of the models for our objects were matter bounded, and as a result produced a large abundance correction factor for N/O in particular. This finding implies that the standard ionization correction factors for the N/O ratio are unsatisfactory when the nebula is optically thin.

Our abundance results show a wide spread in C/O and N/O ratios among the

objects, while He/H, O/H, and Ne/O ranges are much narrower, all of which is consistent with previous studies. In those PNe where more than one line-of-sight position was observed, derived properties were consistent among those positions, thus adding credence to our results and especially our abundance-determining techniques. While our final C/O abundance ratios were determined using collisionally-excited lines, we also estimated values for this ratio using the recombination line C II  $\lambda 4267$ . We found that ratios produced by the latter method are consistently several times greater than those produced by the former, as reported in many studies in the literature.

This project is supported by NASA grant NAG 5-2389. K.B.K. also acknowledges support from a Cottrell College Science grant of Research Corporation and from the Bronfman Science Center and the Dean of Faculty Office at Williams College. R.B.C.H. is grateful to the University of Oklahoma for support of travel to KPNO. We thank Cathy Imhoff, Walter Feibelman and Fred Bruhweiler for help tracking down IUE positional information. We thank Jackie Milingo (OU) and Tim McConnochie (Williams '98) for their assistance with the observations. We are grateful to KPNO for funding McConnochie's observing trip. We also thank the ever-helpful KPNO staff, especially Ed Carder and Jim De Veny.

#### A. Determination of the Merging Factor

The optical and IUE observations were made using slits of different sizes. Due to this, as well as to inherent differences in the two instruments and data-reduction algorithms, one needs to determine a merging factor at each location, i.e. a number by which the UV line strengths are multiplied in order to correct for a systematic offset in the two flux-calibrated spectra for each nebular location.

Calculating a merging factor requires that we know both the observed and theoretical

values of a ratio involving two emission lines, one appearing in the UV and the other in the optical, but produced by the same ion. The merging factor is obtained by dividing the theoretical by the observed ratio.

Two such ratios are He II  $\lambda 1640$ /He II  $\lambda 4686$  and C III]  $\lambda 1909$ /C II  $\lambda 4267$ . We measured the values of one or both of these ratios in all of our target positions. The theoretical values for the He line ratio were determined using recombination results in Storey & Hummer (1995) along with necessary electron temperatures and densities inferred from our optical observations. The theoretical carbon line ratios were determined using the empirical fit in Kaler (1986). Because of the dependence of the C III]/C II ratio on the generally weak C II  $\lambda 4267$  recombination line as well as the temperature-sensitive collisionally-excited C III]  $\lambda 1909$  line, the temperature-insensitive He ratio was preferred for determining the merging factor. Thus, when joining UV and optical spectra, the carbon ratio was employed only in those cases when He II  $\lambda 1640$  was not observed. Merging factors for NGC 7009, NGC 6720, and NGC 6210 were computed from the helium lines, while for IC 3568, IC 4593, and NGC 6826 the carbon lines were employed.

We note that for those objects for which both ratios were available, we found good consistency between the two factors. This is shown in Fig. A1, where we plot the merging factor determined from the helium lines versus that from the carbon lines for those nebular positions where both factors could be calculated. The solid line shows where points would lie if factors at each location were equal. Clearly, the He factor tends to be systematically larger than the C factor but for reasons that are not obvious. It is possible that this offset is related to the tendency to overestimate the strength of a weak line such as C II  $\lambda 4267$ . However, there is good evidence here overall for rough agreement in merging factors, a result which supports the use of each of these factors. We believe that this is the first time that the carbon lines have been used in this manner to combine UV and optical spectra.

The merging factor used to scale data at each location is given in the last row of Table 2. If the IUE and Goldcam slits had overlapped perfectly, then the value of the merging factor should be unity, ignoring instrumental effects. Since the ratio of slit areas was 1:2 (Goldcam:IUE), then we would expect merging factors to fall within roughly a factor of 2 of unity. However, results in Table 2 show that this number is below 0.3 for six of our 13 positions measured. In attempting to understand the cause of these low merging factors, we considered such things as quality of slit overlap, as discussed in §2.3, the particular line ratio used to determine the merging factor, excitation level of the object, electron density, and whether or not the position appears to be matter-bounded. For example, although we believe the slit overlap for IC 3568 to be good, the merging factor is unexpectedly low. Likewise, the quality of slit position match-up for the other five positions with merging factors below 0.3 is “reasonably good.” In addition, for four of the six positions in question, the merging factor was determined using the carbon ratio, thus it is not obvious that the technique used to determine the merging factor is itself at fault. Using the [O II]/[O III] line ratio as an indicator of excitation, we find no clear excitation difference between the six positions with low merging factors and those with values closer to unity. Nor does any pattern emerge when either electron density or the question of matter-boundedness is considered. Curiously, however, all of the merging factors differing significantly from unity are also *less than* unity, indicating that fluxes measured with the IUE are consistently too large with respect to the optical fluxes, even after accounting for the factor-of-two difference in slit area. While this might be indicative of calibration problems with one of the instruments, we would also expect the effect to appear at all other positions as well, which is not the case.

Alas, there appears to be no obvious connection between these properties and the calculated merging factor, and thus we are forced to conclude that, while in most instances the slit overlap appears to have been good, the smaller area of the Goldcam slit may

have frequently sampled regions with lower surface brightness, perhaps by excluding knots present in the IUE slit. However, we argue that given the apparent consistency between the He and C merging factors shown in Fig. A1, their use in joining the UV and optical spectra for the current objects is justified and is no doubt better than applying no correction at all.

We plan to pursue the question of merging factors using a larger database in a future paper.

## REFERENCES

- Acker, A., Ochsenbein, F., Stenholm, B., Tyllenda, R., Marcout, J., & Schohn, C. 1992, The Strasbourg-ESO Catalogue of Galactic Planetary Nebulae, (Garching bei München: ESO)
- Bohigas, J., & Olguín 1996, *Rev Mex A&Ap*, 32, 47
- Clegg, R.E.S., Peimbert, M., & Torres-Peimbert, S. 1987, *MNRAS*, 224, 761
- Ferland, G.J. 1990, Ohio State Univ. Rep. 90-02
- French, H.B. 1983, *ApJ*, 273, 214
- Grevesse, N., & Anders, E. 1989, in *Cosmic Abundances of Matter* (AIP Conf. Proc. 183), ed. C.J. Waddington, 1
- Henry, R.B.C., Kwitter, K.B., & Buell, J. 1998, *Rev Mex A&Ap*, in press
- Henry, R.B.C., Kwitter, K.B., & Howard, J.W. 1996, *ApJ*, 458, 215 (Paper I)
- Howard, J.W., Henry, R.B.C., & McCartney, S. 1997, *MNRAS*, 284, 465
- Kaler, J.B. 1986, *ApJ*, 308, 337
- Kwitter, K.B., & Henry, R.B.C. 1996, *ApJ*, 473, 304 (Paper II)
- Péquignot, D., Petitjean, P., & Boisson, C. 1991, *A&A*, 251, 680
- Perinotto, M., 1991, *ApJS*, 76, 687
- Rola, C., & Stasińska, G. 1994, *A&A*, 282, 199
- Savage, B.D., & Mathis, J.S. 1979, *ARA&A*, 17, 73
- Seaton, M.J. 1979, *MNRAS*, 187, 73p

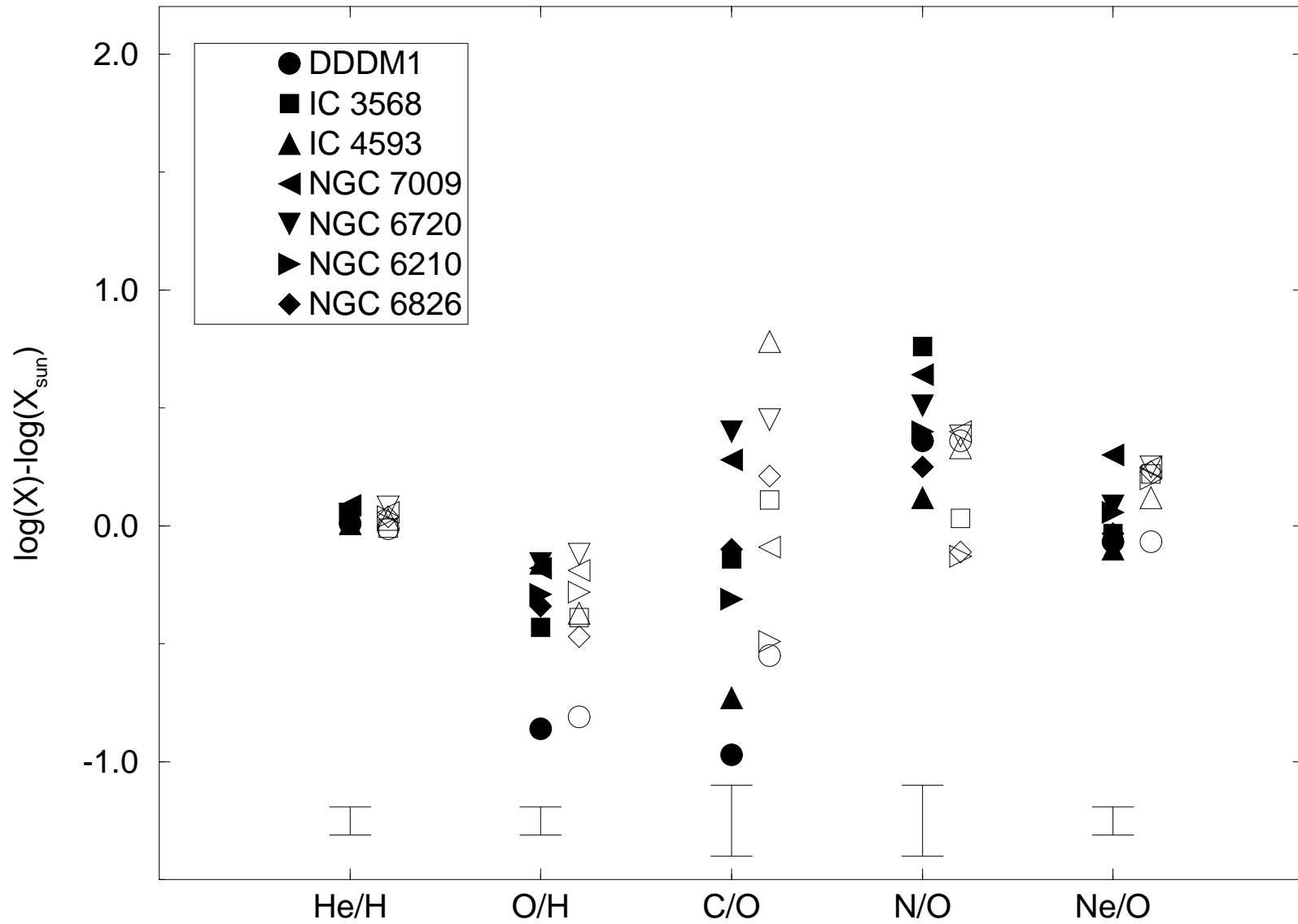
Shields, G., Aller, L.H., Keyes, C.D., & Czyzak, S.J. 1981, ApJ, 248, 569

Storey, P.J., & Hummer, D.G. 1995, MNRAS, 272, 41

Fig. 1.— The five abundance ratios computed here and normalized to their solar values (Grevesse & Anders 1989) are plotted logarithmically. Symbol shapes are used to designate each object (see legend). Filled symbols are our results, while open symbols refer to results from other studies found in the literature: values for IC 4593 were taken from Bohigas & Olgúin (1996), C/O for DDDM1 is from Howard et al. (1996) and consistent with the upper limit given in Clegg et al. (1987), all other C/O values are from Rola & Stasińska (1994; their ratios as derived from C III]  $\lambda$ 1909), and all remaining abundance ratios are from Perinotto (1991).

Fig. A1.— Helium merging factor versus carbon merging factor for those nebular positions for which both could be measured. The solid line shows the locus of one-to-one correspondence.

Fig. 1



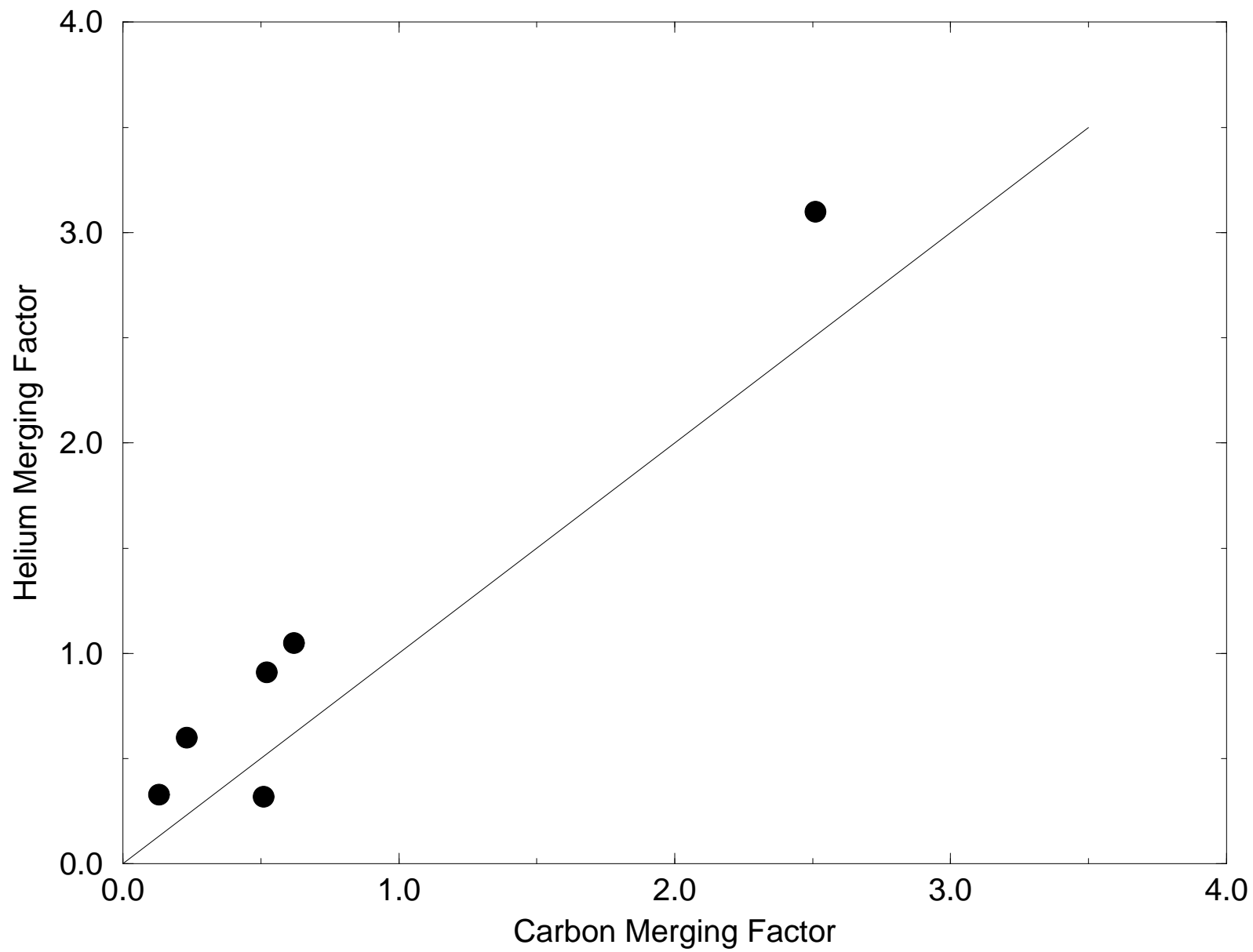


TABLE 1  
FINAL ARCHIVE SPECTRA

Object	SWP	Exposure Time (s)
DDDM1	23872	08100
	39590	06720
	23840	03600
IC 3568	05432	01200
	47015	00900
	47016	00900
IC 4593	33382	01200
	33383	02400
NGC 7009a	45043	00600
NGC 7009b	45047	01800
NGC 7009c	45619	22500
NGC 7009d	45045	01800
NGC 6720a	41639	04800
NGC 6720b	07231	05400
NGC 6210	14650	02100
	14651	02100
NGC 6826a	25255	00480
NGC 6826b	14615	02400
	14616	01200
NGC 6826c	25254	00600

TABLE 2  
UV & OPTICAL LINE STRENGTHS

Line	DDDM1		IC 3568		IC 4593		NGC 7009a		NGC 7009b		NGC 7009c		NGC 7009d		
	f(λ)	F(λ)	I(λ)	F(λ)	I(λ)	F(λ)	I(λ)	F(λ)	I(λ)	F(λ)	I(λ)	F(λ)	I(λ)	F(λ)	I(λ)
C III λ1175	1.85	...	...	...	...	...	...	...	...	...	...	...	...	14	31
N V λ1241	1.64	...	...	...	...	...	...	3.3	5.9	5.7	12	...	...	9.5	18
C II λ1336	1.41	...	...	...	...	...	...	7.5	11	7.8	15	6.8	14	10	16
O IV λ1402	1.31	...	...	...	...	...	...	...	...	...	...	...	...	...	...
N IV λ1485	1.23	...	...	...	...	...	...	...	...	2.4	4.2	...	...	2.4	3.4
C IV λ1549	1.18	...	...	97	21	30	5.8	8.2	9.4	7.7	13	28	36	13	17
[Ne V] λ1575	1.17	...	...	...	...	...	...	...	...	1.7	2.8	73	90	2.2	2.9
He II λ1640	1.14	...	...	...	...	...	...	62	68	44	75	18	21	72	96
O III λ1662	1.13	...	...	14	2.9	...	...	...	...	5.9	10	...	...	7.3	9.7
N III λ1750	1.12	14	15	...	...	...	...	3.4	3.6	4.6	7.8	8.2	9.0	9.0	12
C II λ1760	1.12	...	...	...	...	...	...	...	...	...	...	...	...	...	...
Si II λ1812	1.13	...	...	...	...	...	...	...	...	...	...	...	...	1.9	2.5
Si III λ1887	1.21	4.6	5	...	...	...	...	...	...	...	...	...	...	...	...
C III λ1909	1.23	7.1	8	175	40	12	2.5	51	61	53	94	58	81	64	91
[O II] λ 3727	0.29	103	105	5.2	7.0	37	42	5.5	7.5	11	12	22	41	12	15
He II + H10 λ3797	0.27	4.8	4.9	...	...	...	...	...	...	...	...	...	...	4.0	4.9
He II + H9 λ3835	0.25	6.9	7.0	...	...	...	...	...	...	...	...	...	...	...	...
[Ne III] λ3869	0.25	30	30	57	75	27	29	63	82	84	93	76	133	87	105
He I + H8 λ3889	0.25	19	19	13	17	17	19	14	18	17	18	12	20	17	21
Hε + [Ne III] λ3968	0.23	26	26	27	34	22	24	32	41	41	45	35	58	42	49
He II λ4026	0.21	2.0	2.1	1.6	2.0	1.8	1.9	1.9	2.3	2.2	2.4	...	...	2.1	2.4
[S II] λ4072	0.20	2.6	2.7	0.31	0.38	0.45	0.49	1.5	1.8	1.9	2.1	...	...	2.2	2.5
He II + H8 λ4101	0.19	25	26	20	24	22	24	21	26	24	26	22	33	23	27
He II λ4198	0.16	...	...	...	...	...	...	...	...	...	...	...	...	0.21	0.24
C II λ4267	0.14	...	...	0.24	0.28	0.16	0.17	0.36	0.42	0.73	0.78	...	...	0.50	0.55
Hγ λ4340	0.13	47	48	40	46	44	47	40	45	45	47	38	50	43	47
[O III] λ4363	0.12	5.2	5.3	8.0	9.0	1.8	1.9	6.0	6.8	7.0	7.4	5.3	6.9	6.5	7.1
He I λ4471	0.09	4.8	4.9	4.4	4.8	4.7	4.9	4.7	5.2	5.2	5.4	5.5	6.8	4.7	5.1
He II λ4540	0.07	...	...	...	...	...	...	0.26	0.29	0.36	0.37	...	...	0.43	0.45
N III λ4640	0.05	...	...	1.8	1.9	2.9	2.9	4.8	5.0	5.1	5.2	...	...	4.5	4.7
He II λ4686	0.04	...	...	1.0	1.1	0.66	0.67	1.0	1.1	1.2	1.2	3.0	3.2	1.5	1.5
[Ar IV] λ4711 + He I λ4713	0.03	...	...	...	...	0.58	0.59	4.7	4.9	4.0	4.1	3.0	3.2	3.7	3.8
[Ar IV] λ4740	0.02	...	...	1.9	1.9	...	...	4.3	4.4	3.8	3.8	0.66	0.69	3.5	3.6
Hβ λ4861	0.00	100	100	100	100	100	100	100	100	100	100	100	100	100	100
He I λ4922	-0.02	1.1	1.1	...	...	1.5	1.5	1.7	1.6	1.5	1.4	2.2	2.1	1.4	1.4
[O III] λ4959	-0.03	148	148	370	359	182	180	399	386	402	397	442	414	404	395
[O III] λ5007	-0.04	454	453	1154	1105	565	556	1252	1198	1218	1197	1352	1234	1257	1220
[N I] λ5199	-0.09	0.44	0.44	0.01	0.01	...	...	...	...	0.10	0.10	1.2	1.0	...	...
He II λ5411	-0.13	...	...	...	...	...	...	1.2	1.0	1.1	1.0	...	...	1.3	1.2
[Cl III] λ5517	-0.16	0.21	0.20	0.35	0.30	0.41	0.39	0.56	0.47	0.51	0.48	...	...	0.57	0.51
[Cl III] λ5537	-0.16	0.26	0.26	0.29	0.25	0.37	0.35	0.66	0.55	0.66	0.62	...	...	0.73	0.65
[N II] λ5755	-0.21	1.4	1.4	0.01	0.01	0.10	0.09	0.19	0.15	0.33	0.31	1.1	0.71	0.43	0.37
C IV λλ5801,5812	-0.22	...	...	0.63	0.50	...	...	...	...	...	...	...	...	...	...
He I λ5876	-0.23	15	15	20	16	16	15	20	16	17	15	28	17	17	15
[K IV] λ6101	-0.28	...	...	...	...	...	...	0.35	0.26	...	...	...	...	0.18	0.15
He II λ6116	-0.28	...	...	...	...	...	...	...	...	...	...	...	...	...	...
[O I] λ6300	-0.31	2.4	2.3	...	...	...	...	...	0.28	0.24	4.4	2.2	0.51	0.41	...
[S II] λ6312	-0.31	1.8	1.7	0.44	0.32	0.83	0.73	1.5	1.1	1.7	1.5	...	...	2.0	1.6
[O I] λ6363	-0.32	0.85	0.84	...	...	...	...	...	...	...	...	...	...	0.23	0.18
[Ar V] λ6434	-0.34	...	...	...	...	...	...	...	...	...	...	...	...	...	...
[N II] λ6548	-0.36	18	17	...	...	3.2	2.8	2.2	1.5	5.3	4.5	...	...	7.4	5.7
Hα λ6563	-0.36	292	286	420	289	332	287	423	289	335	287	645	292	372	288
[N II] λ6584	-0.36	54	53	2.5	1.7	12	11	8.6	5.9	17	15	112	50	24	18
He I λ6678	-0.38	4.1	4.0	5.8	3.9	4.5	3.9	6.1	4.0	4.8	4.1	10	4.4	5.1	3.9
[S II] λ6716	-0.39	3.2	3.1	0.15	0.10	0.64	0.55	0.82	0.55	1.4	1.2	13	5.7	2.1	1.6
[S II] λ6731	-0.39	5.4	5.2	0.17	0.11	0.92	0.78	1.4	0.92	2.5	2.1	19	8.1	3.5	2.7
[Ar V] λ7005	-0.43	0.10	0.10	...	...	...	...	...	...	...	...	...	...	...	...
He I λ7065	-0.44	8.1	7.9	6.0	3.8	4.8	4.0	6.6	4.2	5.4	4.5	3.9	1.5	6.6	4.8
[Ar III] λ7135	-0.45	8.1	7.9	12	7.6	12	9.7	21	13	19	15	23	8.3	24	17
[Ar IV] λ7168	-0.46	0.04	0.04	...	...	...	...	0.25	0.15	...	...	...	...	...	...
He II λ7178	-0.46	...	...	...	...	...	...	...	...	...	...	...	...	...	...
[Ar IV] λ7235	-0.47	...	...	...	...	...	...	0.28	0.17	0.34	0.28	...	...	0.35	0.25
He I λ7281	-0.47	0.92	0.90	1.0	0.61	...	...	0.94	0.57	0.70	0.57	...	...	0.88	0.63
[O II] λ7325	-0.48	16	16	1.2	0.74	2.9	2.4	2.5	1.5	2.4	2.0	6.6	2.3	3.1	2.2
[Cl IV] λ7529	-0.51	0.02	0.02	...	...	...	...	0.83	0.48	0.47	0.38	...	...	0.51	0.35
[Ar III] λ7751	-0.54	1.9	1.9	3.0	1.7	2.8	2.3	5.4	3.0	4.5	3.6	6.0	1.8	6.0	4.1
[Cl IV] λ8045	-0.57	...	...	...	...	...	...	2.0	1.1	1.0	0.81	1.4	0.39	1.2	0.81
He II λ8236	-0.59	...	...	...	...	...	...	0.56	0.30	0.37	0.28	...	...	0.53	0.35
P16 λ8467	-0.62	...	...	...	...	...	...	...	...	...	...	...	...	...	...
P15 λ8502	-0.62	...	...	...	...	...	...	...	...	0.56	0.43	...	...	0.72	0.46

TABLE 2—*Continued*

Line	DDDM1			IC 3568		IC 4593		NGC 7009a		NGC 7009b		NGC 7009c		NGC 7009d	
	f( $\lambda$ )	F( $\lambda$ )	I( $\lambda$ )												
P14 $\lambda$ 8544	-0.63	...	...	...	...	0.57::	0.44::	0.99:	0.51:	0.64:	0.49:	...	...	0.89:	0.57:
P13 $\lambda$ 8598	-0.63	...	...	...	...	0.87::	0.67::	1.1:	0.56:	0.73:	0.56:	...	...	0.99:	0.63:
P12 $\lambda$ 8664	-0.64	0.91::	0.88::	1.5::	0.77::	0.88::	0.68::	1.3:	0.66:	1.0:	0.78:	...	...	1.4:	0.89:
P11 $\lambda$ 8750	-0.64	1.1::	1.1:	1.8:	0.93::	1.2:	0.89:	2.0:	1.0:	1.2:	0.90:	3.2:	0.77:	1.8:	1.1:
P10 $\lambda$ 8862	-0.65	1.5:	1.4:	2.4:	1.2:	1.7:	1.3:	2.6:	1.3:	1.5:	1.2:	...	...	2.4:	1.5:
P9 $\lambda$ 9014	-0.67	2.0:	1.9:	3.7:	1.8:	2.0:	1.6:	2.8:	1.4:	1.8:	1.3:	...	...	2.7:	1.7:
[S III] $\lambda$ 9069	-0.67	21:	20:	12:	5.7:	21:	16:	43:	21:	33:	25:	73:	17:	50:	31:
P8 $\lambda$ 9228	-0.68	3.4:	3.3:	6.4:	3.2:	3.4:	2.6:	6.1:	3.0:	3.8:	2.8:	5.2:	1.2:	5.7:	3.5:
[S III] $\lambda$ 9532	-0.70	50:	48:	28:	13:	60:	45:	42:	20:	30:	22:	59:	13:	54:	33:
P7 $\lambda$ 9544	-0.70	4.0:	3.8:	6.1:	2.9:	6.1:	4.6:	5.2:	2.5:	3.2:	2.4:	...	...	3.8:	2.3:
$\log F_{H\beta}$ <sup>a</sup>	-11.78			-11.40		-10.87		-10.87		-10.62		-12.15		-10.62	
c			0.023		0.45		0.18		0.46		0.19		0.95		0.31
merging factor <sup>b</sup>			1.0		0.064		0.12		0.33		1.05		0.09		0.60

<sup>a</sup>Ergs/cm<sup>2</sup>/s in our extracted spectra

<sup>b</sup>Factor by which dereddened UV line strengths are multiplied in order to merge them with optical data (see text).



TABLE 2—CONTINUED—*Continued*

Line	NGC 6720a		NGC 6720b		NGC 6210		NGC 6826a		NGC 6826b		NGC 6826c		
	f( $\lambda$ )	F( $\lambda$ )	I( $\lambda$ )										
[O I] $\lambda$ 6300	-0.31	8.6	8.3	128	93	3.7	3.5	...	...	...	...	...	...
[S III] $\lambda$ 6312	-0.31	1.9	1.8	0.47::	0.34::	1.4	1.3	0.75	0.75	0.72	0.66	1.2	0.92
[O I] $\lambda$ 6363	-0.32	2.7	2.6	43	31	1.1	1.1	0.03::	0.03::	0.04	0.04	...	...
[Ar V] $\lambda$ 6434	-0.34	0.14	0.13	...	...	...	...	...	...	...	...	...	...
[N II] $\lambda$ 6548	-0.36	53	51	428	298	8.8	8.3	1.8	1.8	1.9:	1.7:	4.1	3.0
H $\alpha$ $\lambda$ 6563	-0.36	301	286	416	289	305	287	286	286	317	287	390	288
[N II] $\lambda$ 6584	-0.36	168	160	1370	948	30	29	7.8	7.8	12	11	12	9.0
He I $\lambda$ 6678	-0.38	3.2	3.1	7.7	5.2	4.3	4.0	3.9	3.9	4.4	4.0	5.5	4.0
[S II] $\lambda$ 6716	-0.39	13	12	78	53	2.8	2.6	0.42	0.42	0.52	0.47	0.84	0.61
[S II] $\lambda$ 6731	-0.39	12	12	70	47	4.8	4.5	0.61	0.61	0.73	0.65	1.2	0.84
[Ar V] $\lambda$ 7006	-0.43	0.32	0.30	...	...	...	...	...	...	...	...	...	...
He I $\lambda$ 7065	-0.44	2.4	2.3	8.1	5.2	6.3	5.8	3.5	3.5	4.4	3.9	5.2	3.6
[Ar III] $\lambda$ 7135	-0.45	25	23	45	29	14	12	11	11	12	11	16	11
[Ar IV] $\lambda$ 7168	-0.46	0.06	0.05	...	...	...	...	...	...	...	...	...	...
He II $\lambda$ 7178	-0.46	0.48	0.45	...	...	...	...	...	...	...	...	...	...
[Ar IV] $\lambda$ 7235	-0.47	0.54	0.51	...	...	0.15	0.14	0.57	0.57	0.52	0.46	0.69	0.47
He I $\lambda$ 7281	-0.47	0.44	0.41	...	...	0.79	0.73	...	...	0.77	0.67	0.88	0.59
[O II] $\lambda$ 7325	-0.48	7.3	6.8	47	29	7.5	6.9	1.3	1.3	1.9	1.6	2.1	1.4
[Cl IV] $\lambda$ 7529	-0.51	0.21	0.20	...	...	0.27	0.25	...	...	...	...	...	...
[Ar III] $\lambda$ 7751	-0.54	5.9	5.5	13	7.2	3.3	3.0	2.4	2.5	2.9	2.5	4.1	2.6
[Cl IV] $\lambda$ 8045	-0.57	0.58	0.54	...	...	0.62	0.56	0.12	0.12	...	...	...	...
He II $\lambda$ 8236	-0.59	1.2	1.1	...	...	0.07	0.06	...	...	...	...	...	...
P16 $\lambda$ 8467	-0.62	0.49	0.45	...	...	0.43	0.39	...	...	0.39	0.33	...	...
P15 $\lambda$ 8502	-0.62	0.55:	0.50:	...	...	0.55:	0.50:	...	...	0.52:	0.44:	...	...
P14 $\lambda$ 8544	-0.63	0.52:	0.48:	...	...	0.65:	0.59:	0.47:	0.47:	0.58:	0.49:	1.1:	0.63:
P13 $\lambda$ 8598	-0.63	0.57:	0.52:	...	...	0.73:	0.66:	0.55:	0.55:	0.67:	0.56:	1.1:	0.64:
P12 $\lambda$ 8664	-0.64	0.83:	0.76:	...	...	1.0:	0.90:	0.78:	0.78:	0.89:	0.75:	1.3:	0.79:
P11 $\lambda$ 8750	-0.64	1.2:	1.1:	...	...	1.3:	1.1:	1.2:	1.2:	1.2:	0.99:	2.1:	1.2:
P10 $\lambda$ 8862	-0.65	1.5:	1.3:	...	...	1.5:	1.4:	1.3:	1.3:	1.5:	1.2:	2.4:	1.4:
P9 $\lambda$ 9014	-0.67	1.9:	1.7:	...	...	...	...	1.5:	1.5:	2.0:	1.7:	3.4:	2.0:
[S III] $\lambda$ 9069	-0.67	29:	26:	44:	22:	31:	28:	11:	11:	10:	8.6:	30:	17:
P8 $\lambda$ 9228	-0.68	3.2:	2.9:	5.3:	2.7:	4.0:	3.5:	2.8:	2.8:	3.4:	2.8:	5.4:	3.1:
[S III] $\lambda$ 9532	-0.70	71:	65:	101:	50:	77:	68:	39:	39:	39:	32:	105:	58:
P7 $\lambda$ 9544	-0.70	3.8:	3.5:	6.3::	3.1::	4.6:	4.1:	3.5:	3.5:	4.3:	3.6:	7.6:	4.2:
$\log F_{H\beta}$ <sup>a</sup>		-11.68		-12.65		-10.52		-10.96		-10.93		-11.33	
c			0.060		0.44		0.075		0.00		0.12		0.36
merging factor <sup>b</sup>			0.91		0.032		3.1		0.34		0.18		0.055

<sup>a</sup>Ergs/cm<sup>2</sup>/s in our extracted spectra

<sup>b</sup>Factor by which dereddened UV line strengths are multiplied in order to merge them with optical data (see text).

TABLE 3  
ELECTRON TEMPERATURES & DENSITIES

Object	$T_{[OIII]}(K)$	$T_{[NII]}(K)$	$T_{[OII]}(K)$	$T_{[SII]}(K)$	$N_{[SII]}(cm^{-3})$
DDDM1	11,900	12,000	...	...	3300
IC 3568	10,500	6900	...	...	900
IC 4593	8200	7700	12,200	...	1700
NGC 7009a	9400	12,100	...	...	2900
NGC 7009b	9600	10,800	...	...	3200
NGC 7009c	9300	9100	11,500	...	1900
NGC 7009d	9400	10,700	...	...	2900
NGC 6720a	10,400	9900	12,100	...	500
NGC 6720b	10,200	9600	10,500	12,600	400
NGC 6210	9400	10,900	...	...	3200
NGC 6826a	8800	8700	11,100	...	1900
NGC 6826b	9000	9500	11,800	...	1700
NGC 6826c	9000	8900	15,200	...	1700

TABLE 4A  
OBSERVATIONS & MODELS

	DDDM1		IC 3568		IC 4593		NGC 7009a		NGC 7009b		NGC 7009c		NGC 7009d	
	Obs	Model	Obs	Model	Obs	Model	Obs	Model	Obs	Model	Obs	Model	Obs	Model
$\log (I_{[OII]} + I_{[OIII]})/H\beta$	0.86	0.78	1.18	1.27	0.90	1.08	1.21	1.25	1.21	1.16	1.23	1.15	1.22	1.12
$\log I_{[OII]}/I_{[OIII]}$	-0.77	-0.76	-2.33	-2.35	-1.25	-1.24	-2.33	-2.33	-2.12	-2.19	-1.60	-1.56	-2.03	-2.02
$\log I_{HeII}/HeI$	...	-2.78	-1.16	-1.21	-1.34	-2.06	-0.17	-0.25	-0.12	-0.21	-0.71	-0.56	-0.0064	0.08
$\log I_{\lambda 4363}/I_{\lambda 5007}$	-1.93	-1.97	-2.09	-1.93	-2.47	-2.45	-2.25	-2.08	-2.21	-2.17	-2.25	-2.19	-2.23	-2.21
$\log I_{\lambda 6716}/I_{\lambda 6731}$	-0.23	-0.23	-0.053	-0.074	-0.15	-0.03	-0.23	-0.22	-0.24	-0.22	-0.15	-0.22	-0.23	-0.22
$\log I_{He I}/H\beta$	-0.82	-0.85	-0.80	-0.77	-0.83	-0.77	-0.81	-0.75	-0.82	-0.76	-0.78	-0.74	-0.83	-0.79
$\log I_{6584/3727}$	-0.29	-0.28	-0.61	-0.58	-0.60	-0.53	-0.11	-0.15	0.079	-0.016	0.08	0.09	0.08	0.05
$\log I_{6724/3727}$	-1.10	-1.04	-1.52	-1.51	-1.51	-1.55	-0.71	-0.79	-0.56	-0.59	-0.48	-0.47	-0.56	-0.47
$\log I_{1909/5007}$	-1.75	-1.67	-1.44	-1.50	-2.35	-2.31	-1.29	-1.34	-1.10	-1.08	-1.18	-1.06	-1.13	-1.05
$\log I_{3869/5007}$	-1.17	-1.13	-1.17	-1.21	-1.28	-1.31	-1.16	-1.11	-1.11	-1.12	-0.97	-0.94	-1.07	-1.05
Model Input Parameters														
$T_{eff}$ ( $10^3K$ )		40		41		40		77		77		77		77
$\log L/L_{\odot}$		5.81		9.84		7.36		4.99		4.24		4.24		3.34
$N_e$		4000		1000		600		3200		3200		3200		3200
$R_o$ (pc)		0.032		0.032		0.032		0.032		0.032		0.032		0.032
$R$ (pc)		0.35		4.9 <sup>a</sup>		1.8 <sup>a</sup>		0.17 <sup>a</sup>		0.10 <sup>a</sup>		0.13 <sup>a</sup>		0.047 <sup>a</sup>
He/H		0.096		0.11		0.11		0.13		0.13		0.13		0.13
O/H ( $\times 10^4$ )		1.07		2.57		6.46		4.27		4.27		4.27		4.27
C/O		0.063		0.15		0.085		0.43		0.85		0.78		1.58
N/O		0.30		0.40		0.26		0.46		0.52		0.52		0.52
Ne/O		0.14		0.11		0.12		0.14		0.14		0.22		0.17
S/O		0.057		0.038		0.014		0.038		0.048		0.048		0.048

<sup>a</sup>Matter bounded models

TABLE 4A-CONTINUED  
OBSERVATIONS & MODELS

	NGC 6720a		NGC 6720b		NGC 6210		NGC 6826a		NGC 6826b		NGC 6826c	
	Obs	Model	Obs	Model	Obs	Model	Obs	Model	Obs	Model	Obs	Model
$\log (I_{[OII]} + I_{[OIII]})/H\beta$	1.27	1.41	1.26	1.26	1.18	1.08	1.00	1.09	1.00	1.09	1.00	1.07
$\log I_{[OII]}/I_{[OIII]}$	-0.93	-0.93	+0.17	+0.21	-1.51	-1.51	-1.63	-1.61	-1.63	-1.61	-1.71	-1.60
$\log I_{HeII}/HeI$	+0.62	+0.61	-0.87	+0.23	-1.12	-1.21	...	-1.54	...	-1.54	...	-1.55
$\log I_{\lambda 4363}/I_{\lambda 5007}$	-2.09	-2.01	-2.12	-2.18	-2.23	-2.17	-2.33	-2.28	-2.33	-2.28	-2.32	-2.30
$\log I_{\lambda 6716}/I_{\lambda 6731}$	+0.014	+0.025	-0.049	+0.047	-0.24	-0.28	-0.16	-0.17	-0.16	-0.17	-0.14	-0.17
$\log I_{He I}/H\beta$	-0.98	-0.94	-0.75	-0.77	-0.81	-0.76	-0.83	-0.78	-0.83	-0.78	-0.82	-0.78
$\log I_{6584/3727}$	-0.086	-0.051	-0.062	-0.021	-0.20	-0.11	-0.48	-0.39	-0.48	-0.39	-0.33	-0.38
$\log I_{6724/3727}$	-0.92	-0.88	-1.04	-0.99	-0.80	-0.88	-1.35	-1.33	-1.35	-1.33	-1.13	-1.17
$\log I_{1909/5007}$	-0.64	-0.57	-0.66	-0.58	-1.58	-1.50	-1.52	-1.50	-1.52	-1.50	-1.61	-1.53
$\log I_{3869/5007}$	-1.01	-0.96	-0.55	-0.51	-1.08	-0.98	-1.19	-1.16	-1.19	-1.16	-1.22	-1.16
Model Input Parameters												
$T_{eff}$ ( $10^3$ K)		150		150		60		50		50		50
$\log L/L_{\odot}$		5.33		1.12		4.11		5.27		5.27		5.27
$N_e$		500		500		6300		1900		1900		1900
$R_o$ (pc)		0.032		0.032		0.032		0.032		0.032		0.032
$R$ (pc)		0.87		0.072		0.076 <sup>a</sup>		0.28 <sup>a</sup>		0.28 <sup>a</sup>		0.28 <sup>a</sup>
He/H		0.12		0.12		0.12		0.11		0.11		0.11
O/H ( $\times 10^4$ )		7.23		6.76		3.39		4.27		4.27		4.27
C/O		1.20		1.02		0.23		0.34		0.34		0.34
N/O		0.39		0.35		0.32		0.26		0.26		0.26
Ne/O		0.18		0.18		0.20		0.14		0.14		0.14
S/O		0.011		0.01		0.029		0.013		0.013		0.019

<sup>a</sup>Matter bounded models

TABLE 4B  
CORRECTION FACTORS ( $\xi$ )

Object	He/H	O/H	C/O	N/O	Ne/O
DDDM1	0.98	0.89	0.74	1.32	0.91
IC 3568 <sup>a</sup>	0.89	0.82	1.40	2.76	0.88
IC4593 <sup>a</sup>	0.88	0.94	0.95	2.58	0.87
NGC 7009a <sup>a</sup>	0.90	0.91	1.57	1.69	0.84
NGC 7009b <sup>a</sup>	0.93	0.90	1.30	1.61	0.83
NGC 7009c <sup>a</sup>	0.91	0.89	1.03	1.28	0.81
NGC 7009d <sup>a</sup>	0.92	0.83	1.05	1.50	0.81
NGC 6720a	0.92	0.88	0.97	0.83	0.78
NGC 6720b	0.76	0.82	0.49	0.84	0.25
NGC 6210 <sup>a</sup>	0.91	0.89	0.91	1.45	0.82
NGC 6826a <sup>a</sup>	0.90	0.88	0.97	1.88	0.84
NGC 6826b <sup>a</sup>	0.90	0.88	0.97	1.88	0.84
NGC 6826c <sup>a</sup>	0.90	0.88	0.97	1.87	0.84

<sup>a</sup>Matter bounded models

TABLE 5A  
DERIVED ABUNDANCES

Object	He/H	O/H( $\times 10^{-4}$ )	C/O	N/O	Ne/O	Type
DDDM1	0.10	1.17	0.046	0.30	0.12	Halo
IC 3568	0.11	3.14	0.31	0.75	0.13	II-III
IC 4593	0.10	5.95	0.080	0.17	0.11	III
NGC 7009a	0.11	5.76	0.81	0.50	0.14	
NGC 7009b	0.12	5.34	0.94	0.66	0.15	
NGC 7009c	0.12	5.82	0.70	0.52	0.21	
NGC 7009d	0.11	5.46	0.77	0.61	0.17	
NGC 7009(average)	0.12	5.60	0.81	0.57	0.28	II-III
NGC 6720a	0.11	6.35	1.47	0.49	0.17	
NGC 6720b	0.11	5.52	0.71	0.35	0.16	
NGC 6720(average)	0.11	5.94	1.09	0.42	0.17	II-III
NGC 6210	0.11	4.40	0.21	0.33	0.16	II-III
NGC 6826a	0.10	3.97	0.38	0.19	0.14	
NGC 6826b	0.10	3.86	0.32	0.23	0.13	
NGC 6826c	0.10	3.81	0.31	0.28	0.13	
NGC 6826(average)	0.10	3.88	0.34	0.23	0.13	II-III
Sun <sup>a</sup>	0.098	8.51	0.43	0.13	0.14	

<sup>a</sup>Grevesse & Anders (1989)

TABLE 5B  
C/O FROM RECOMBINATION

Object	$\frac{N(C^{+2})_{\lambda 4267}}{N(C^{+2})_{\lambda 1909}}$	C/O
DDDM1	...	...
IC 3568	3.27	1.01
IC 4593	3.12	0.25
NGC 7009a	1.29	1.04
NGC 7009b	1.90	1.79
NGC 7009c	...	...
NGC 7009d	1.21	0.93
NGC 7009 (average)		1.25
NGC 6720a	1.84	2.70
NGC 6720b	5.15	3.66
NGC 6720 (average)		3.18
NGC 6210	2.65	0.56
NGC 6826a	2.87	1.09
NGC 6826b	3.17	1.01
NGC 6826c	3.27	1.01
NGC 6826 (average)		1.04